Journal of Fluids and Structures (2000) **14,** 469–488
doi:10.1006/jfls.1999.0282, available online at http://www.idealibrary.com on IDEAL®

EFFECTS OF LID-DRIVEN CAVITY SHAPE ON THE FLOW ESTABLISHMENT PHASE

C. Migeon, A. Texier and G. Pineau

Laboratoire d'Etudes Aérodynamiques (LEA), Université de Poitiers - C.N.R.S. UMR 6609- Bd. Marie et Pierre CURIE, Téléport 2 - BP 30179, 86960 FUTUROSCOPE Cedex, France

(Received 11 February 1998, and in final form 2 November 1999)

Experiments are carried out to study the flow establishment phase inside closed cavities submitted to the impulsive translation, from rest, of one of their walls at a Reynolds number of 1000. Three standard industrially machined or molded cylindrical cavity shapes are studied and are compared with respect to the efficiency of mixing process: square, rectangular and semi-circular of length-to-width ratio of 2:1. The flow structures in the mid-cross-section are analysed by means of fine topological and kinematic visualization series using two complementary techniques: continuous dye filament and discrete solid tracers both coupled with a laser sheet illumination. Particular attention is given to vorticity propagation and primary/secondary eddy formations. Although a roughly similar vortex generation is observed in all examined cavities, important differences appear with time. The semi-circular cavity flow results in a much more homogeneous and uniform recirculation with no secondary flow recirculation zone. On the contrary, the square and rectangular cavity flows develop a better flow mass dispersion and, respectively, one and two secondary eddies. At the final time of observation ($t^* = 12$), both semi-circular and rectangular cavity flows seem to reach their steady state whereas the square one continues to evolve. Comparisons with 2-D computational results of other authors illustrate the three-dimensional flow aspect present in experiments.

1. INTRODUCTION

Owing to their broad range of natural, industrial and biomedical applications, cavity flows have been studied for years by both experimental and numerical investigations. However, very few of them, specially in the experimental domain, have been conducted on the unsteady flow establishment phase. This shortfall in experimental results is especially regrettable for the validation of unsteady numerical models.

This paper intends to fill in this gap by focusing its attention on closed cavity recirculation. The flow inside the cavity is generated by the translation of one cavity wall referred to as the moving lid. This particular configuration, conventionally named lid-driven cavity (LDC), is considered, according to Koseff & Street (1984a–c), as a "more controlled problem with fewer external factors affecting the state of the flow". Simple in geometry with well-defined boundary conditions, LDC flows are standard references for testing the accuracy of numerical codes (Deville *et al.* 1992), as well as constituting "an ideal vehicle for studying complex flow physics" (Freitas & Street 1988) such as thermocapillary flow stability (Ramanan & Homsy 1994). Parallel to the fundamental case, LDC flow studies are also useful to improve many practical application prototypes (Aidun *et al.* 1991); short-dwell coaters and melt-spinning processes in forming continuous metal ribbons are examples of such applications (Aidun & Triantafillopoulos 1990). So, LDC flow studies are of particular interest for Fluid mechanics investigators, applying their knowledge on fundamental closed-streamline flow as well as improving manufacturing systems efficiency.

0889–9746/00/050469 + 20 $35.00/0

Published results from steady LDC simulations (experimental and numerical) have led to a good understanding of the fully developed flow structures, especially for the cylindrical square section cavity [Koseff & Street (1984a–c), Ghia *et al.* (1982), Freitas *et al.* (1985), among others]. For Reynolds numbers from 1000 to 10 000, the cross-section steady flow of the square cavity (Figure 1) is basically characterized by a large primary eddy (PE), a downstream secondary eddy (DSE), an upstream secondary eddy (USE) and a lower secondary eddy. In spanwise views, experimental and numerical investigations have shown the presence of vortices classified by Prasad & Koseff (1988) as local and global flow features. The local eddies, the so-termed corner vortices, located close to the cavity span end-walls, take a large part in spanwise fluid transport (Chiang *et al.* 1997). The global eddies, commonly referred to as Taylor–Goertler-like vortices, are represented by several dispersed counter-rotating vortex pairs (depending on flow regime and cavity spanwise ratio) which can meander along cavity span (Koseff & Street 1984c). Authors contended that they are the consequence of flow instabilities developed near the concave-separated streamline between the PE and the DSE (Freitas & Street 1988).

In spite of extensive investigations on LDC flows, it may be noted that three major points remain unexplored, as follows.

(i) Very little is known on the unsteady flow establishment phase, rightly named "start-up flow" by Koseff & Street (1982, 1984a–c). However, studying this peculiar phase is of great interest to bring to light the generation process of vortices, with the objective, in view of flow control, to reduce or increase their development towards the fully established state.
(ii) Only a tiny bit is known about the cavity shape influence on birth and evolution of recirculating flow structures.
(iii) Little is known on mixing flow, in spite of its practical importance, especially in industrial mixing process (Middleman 1977).

How the cavity shape influences the initial phase of the flow establishment is the focal point of this paper. Three cavity shapes are studied: the classical square one, a steep rectangular one and a semi-circular one. The first stages of mixing process are looked into. In order to better describe the birth and development of both primary and secondary eddies, topological and kinematic points are particularly examined: eddy coordinates,

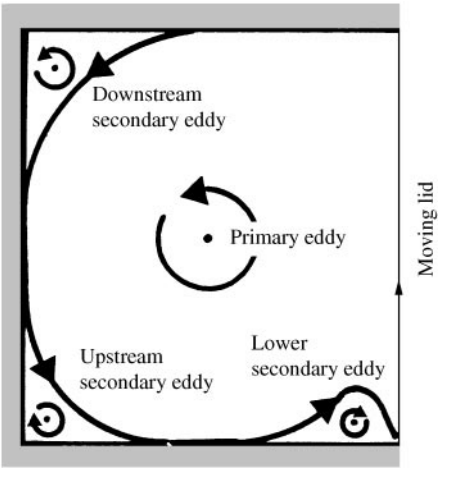

Figure 1. Sketch of the fully developed cross-sectional flow in the square-cavity.

secondary eddy dimensions and velocity profiles. These data will constitute a useful experimental benchmark for comparisons with numerical and experimental results.

2. EXPERIMENTAL ARRANGEMENT

2.1. Recirculation Generating

Experiments were carried out on a modified version of an extensively presented experimental apparatus, especially set up to study the first stages of hydrodynamic flow evolution around impulsively started obstacles (Boisaubert *et al.* 1996). A diagrammatic view of the experimental arrangement is given in Figure 2.

In previously quoted experimental LDC works, the recirculating motion is induced by a moving lid simulated by a belt (Koseff & Street 1982,1984a–c) or a cylinder (Pan & Acrivos 1966) placed at the top of a fixed cavity. In this experimental investigation, the cavity, towed in a vertical water tank ($80 \times 100 \times 120$ cm^3 capacity), slides smoothly downward along a large fixed vertical plate acting as a lid. Flow development is sequentially

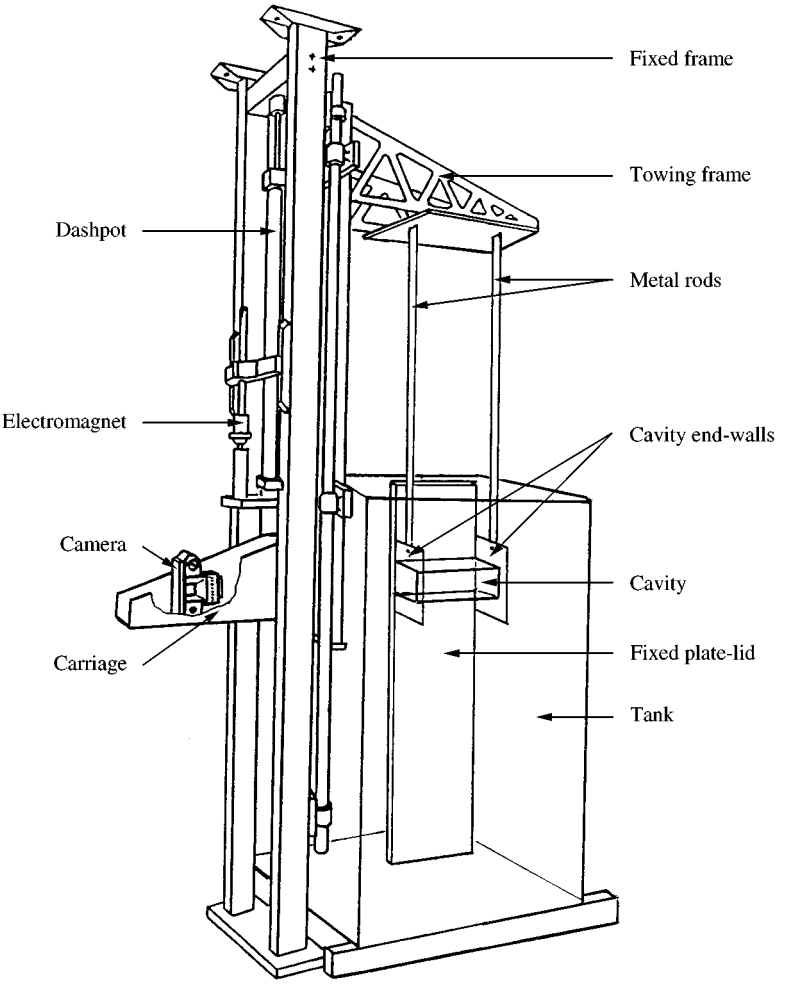

Figure 2. Experimental set-up.

recorded at regular dimensionless time-step $\Delta t^* = 1 (t^* = tV_0/B;\ 0 \leq t^* \leq 12)$, by a computer-controlled camera positioned on the cavity-accompanying carriage, so that the cavity appears to be fixed in the camera frame and the plate as the moving lid. For all submitted pictures, taken at least twice for reliability, the relative lid motion is upward.

The spanwise cavity extremities are bounded with end walls linked to the towing frame by means of metal rods which maintain cavity horizontality and guide its fall. Spring-leaves, located at the cavity end extremities, maintain continuous contact between the "plate lid" and the cavity itself without any escape of fluid. To allow visualization, the tank and the cavity walls are made of altuglass and both filled with water. Before an experiment, the cavity-support carriage is linked to the fixed frame by an electromagnet until the fluid comes to rest. At the initial moment, the system is abruptly released (under gravity and retarding dashpot force) with a constant speed V_0, fitted by the adjustment of the dashpot fluid escape. In this study, the cavity velocity ($V_0\mathbf{x}$), or the relative velocity lid ($-V_0\mathbf{x}$), is equal to 1·8 cm/s in magnitude, defining a Reynolds number of 1000 [$\mathrm{Re} = V_0 B/\nu$, in which B is the cavity width and ν is the kinematic viscosity of the fluid (water)].

Experiments were performed inside three cylindrical cavities (square, rectangular and semi-circular ones) 12·4 cm in length (L) and 6·2 cm in width (B), defining a length-to-width aspect ratio of 2:1. Cavity boundary nomenclature and reference frame are given in Figure 3.

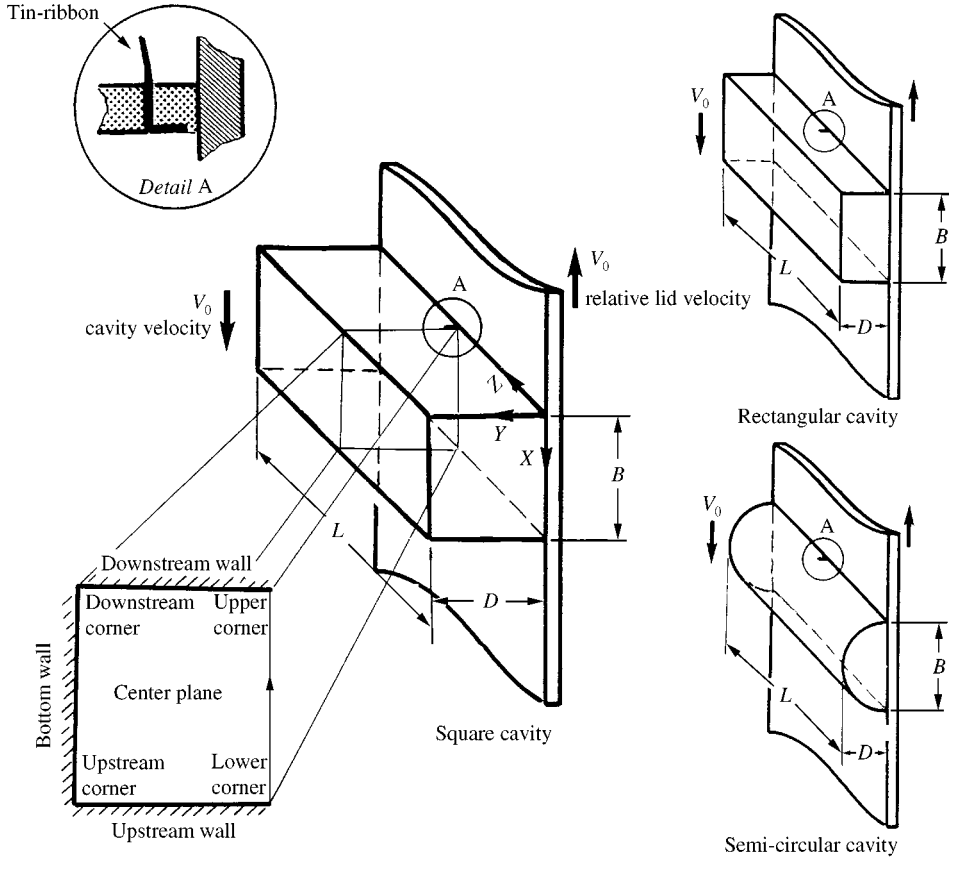

Figure 3. Cavity nomenclature and reference frame.

2.2. Flow Visualization Techniques

Flow analysis is made in the cavity centre-plane ($Z/L = \frac{1}{2}$) by means of two complementary visualization techniques both coupled with a laser sheet illumination.

The first technique is a continuous dye-emission one. The dye is generated by the electrolysis of a piece of tin-ribbon (5 mm in length) located in a groove tooled in the downstream-wall cavity, 2 mm downstream the upper corner (Figure 3, detail A). A DC voltage in the order of 20 v is applied between the wire (anode), coming from a downstream cavity hole, and a copper sheet (cathode) immersed in the tank area. When the lid starts, the nascent cavity flow-stream "absorbs" the "smoke" emitted from the tin-ribbon wall, giving information on the first stages of vorticity convection. Figure 4 shows selected pictures obtained with this dye-filament technique for the three studied cavity shapes.

The second technique is a solid tracer one. Lighted particles, correctly seeded in the cavity area, are recorded with a suitable time of exposure to obtain instantaneous streak fields which, after analysis, deliver information on both flow topology and kinematics. Figure 5 depicts the time evolution of such particle-streak pictures. Velocity fields are deduced by meticulous measurements of the particle marks on enlarged negatives; the relative accuracy is better than 3%.

3. EXPERIMENTAL RESULTS

3.1. General Description of the Start-up Flow: Flow Structures and Parameters

At rest, the initial velocity and vorticity fields are nil in all cavity areas. As soon as the lid is set in relative upward motion, high shear stress develops along the cavity lid. Dragged to the upper corner and deflected by the downstream wall, the high-vorticity fluid penetrates the quiescent cavity fluid in the shape of a counter-clockwise-rotating primary structure which grows with time (Figures 4 and 5). From $t^* = 4$, the rectangular- and square-cavity flows give birth to additional clockwise-rotating secondary eddies, whereas, for the semi-circular case, only the main eddy develops up to the final visualized time $t^* = 12$. The magnified streamline sketches of secondary eddies depicted in Figure 5 provide clues on the precise localization of divided streamlines. As Koseff & Street (1984) clearly mentioned, the flow separation is due to the combined effects of pressure increase close to the corner and of wall-jet frictional-deceleration upstream this corner. The wall jet cannot thwart the pressure gradient; a flow separation is induced, giving birth to a secondary recirculation.

The primary eddy (PE) and the two secondary eddies (SE), respectively, located near the *D*ownstream and the *U*pstream corners, are distinguished from each other with the general literature abbreviations DSE/USE, set in an additional subscript letters form with reference to the cavity shape. For instance, $\text{semi-circular}_{\text{PE}}$ stands for the primary eddy which develops in the semi-circular cavity. As previously specified, and as will be used in Section 3.2, pictures are accurately analyzed in order to deduce flow geometrical parameters (Figure 6). Dye-filament visualizations (Figure 4) are central to the understanding of the mixing process and to providing information about the redistribution mechanism of the vorticity produced on the lid. As a function of the cavity shape, the development of the dye-filament has been characterized by its dimensionless stretch, $S_{th} = d/b$, and surrounded area, $A = A_{\text{dye-filament}}/A_S$, where d and b, respectively, represent the depth-space and width-space of the dye-filament rolling-up (Figure 6), and, $A_{\text{dye-filament}}$ and A_s, are respectively, the delimited dye-filament area and the reference square-cavity area. The secondary eddy dimensions and vortex-core positions, considered by Koseff & Street (1984a–c) as "a useful benchmark" for result comparisons, are measured from particle-streak visualizations

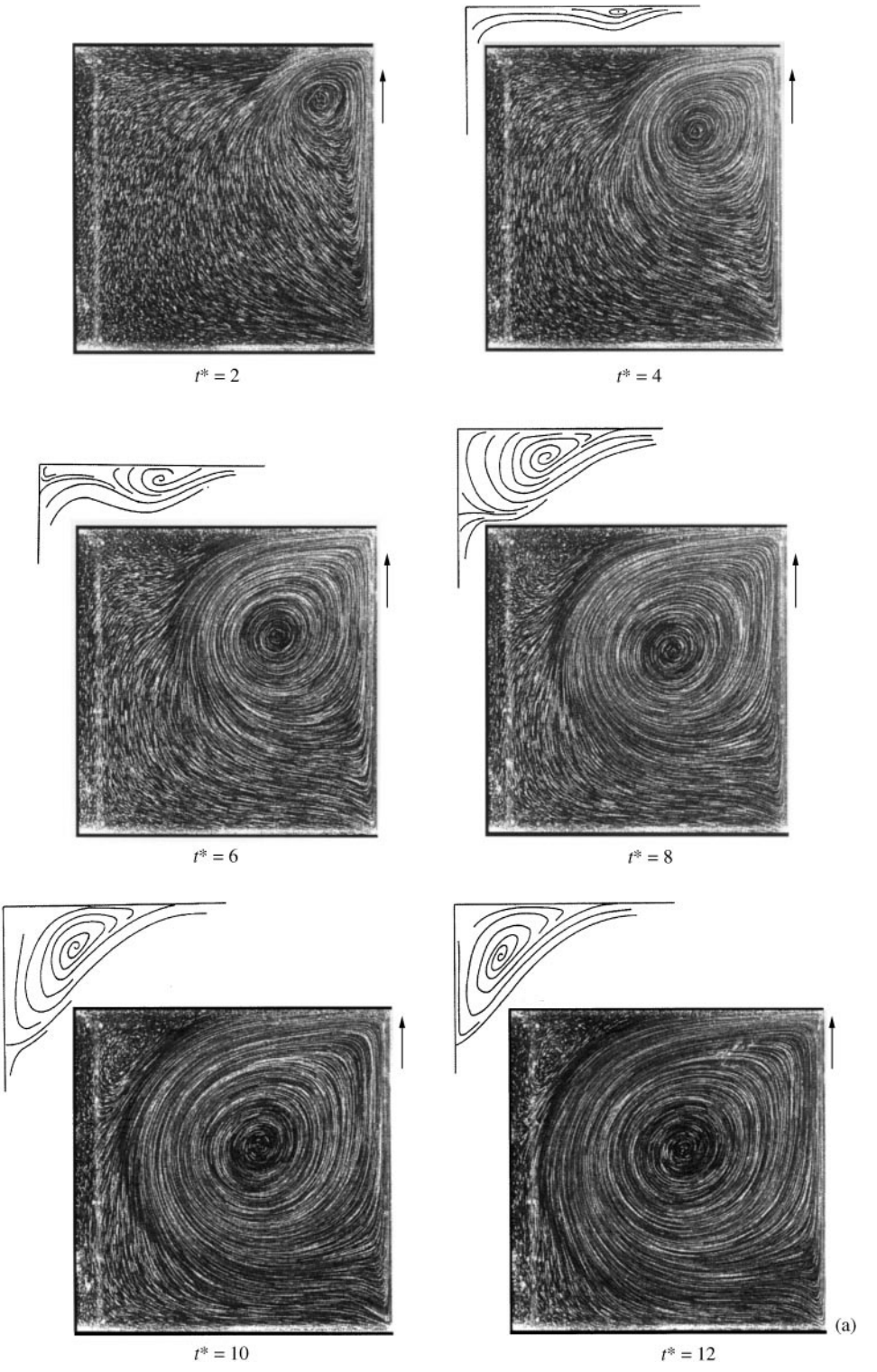

Figure 5. Particle-streak picture time evolutions: (a) square cavity; (b) rectangular cavity; (c) semi-circular cavity.

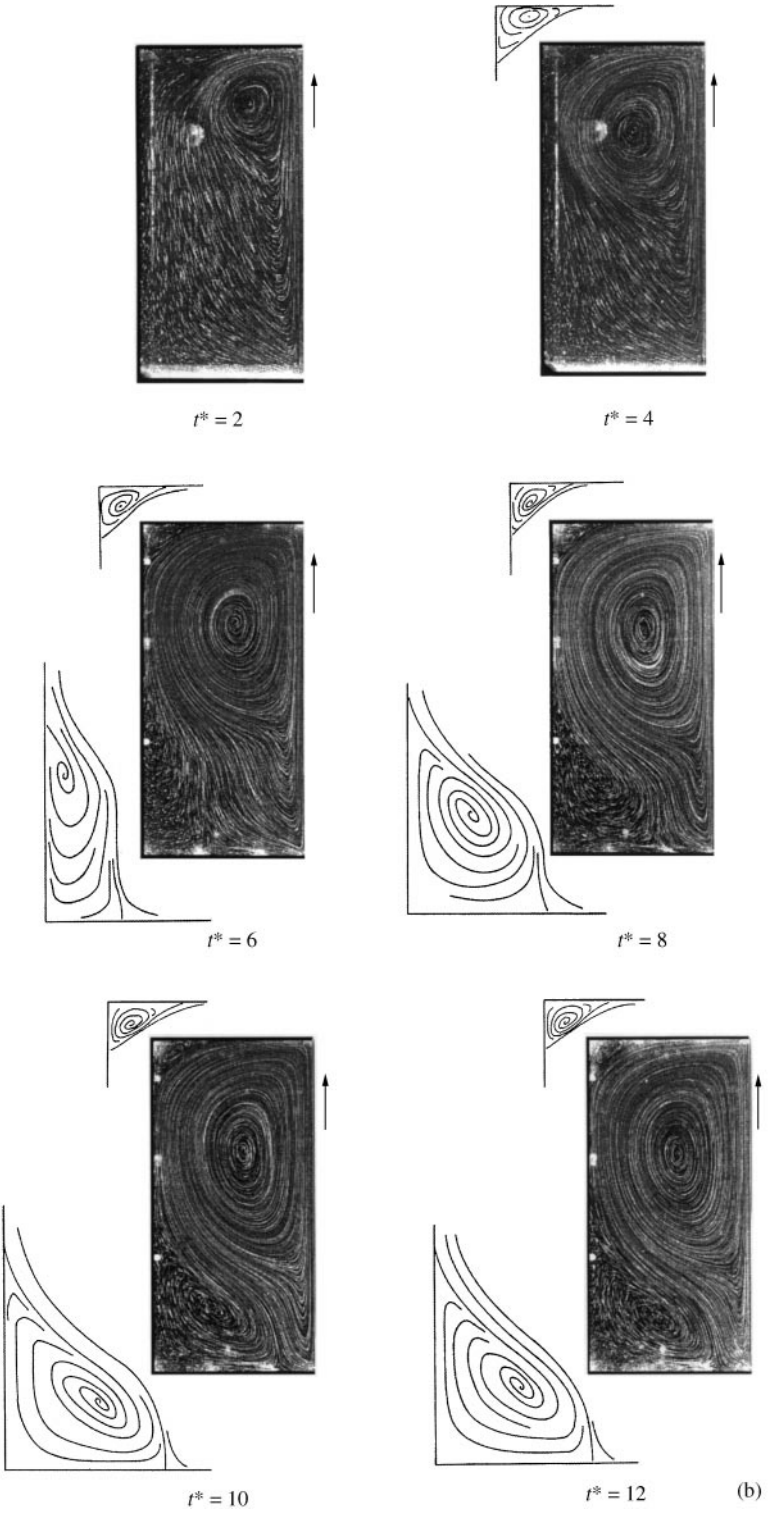

Figure 5. continued

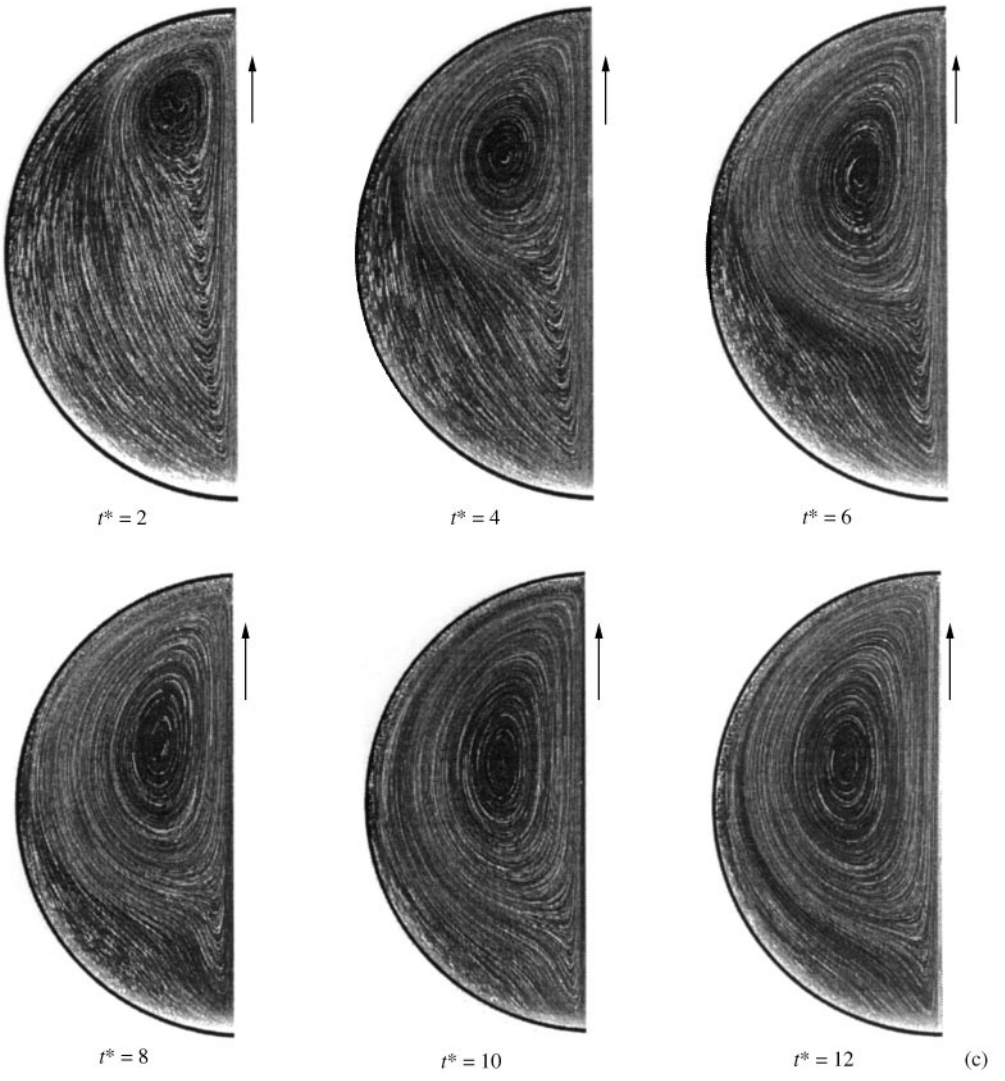

Figure 5. continued

(Figure 5). Secondary eddy dimensions (Figure 6) are sized from each downstream- and upstream corner to the separation point on both downstream and bottom walls for the DSE (square and rectangular cavity cases) and on both bottom and upstream walls for the USE (rectangular cavity case). For instance, D_Y-rectangular$_{\mathrm{DSE}}$ is the rectangular$_{\mathrm{DSE}}$ Y-axis size, and D_X-rectangular$_{\mathbf{DSE}}$ is its X-axis dimension. Localization of vortex cores (main and secondary) is given in (X, Y) coordinate forms in the (oxy) reference frame.

In the kinematic part (Section 3.3), for the three studied cavity shapes, velocity profiles have been measured along the primary eddy centrelines (CX) and (CY), but also, in order to make comparisons with the fully established state (Ghia *et al.* 1982), along the traditional square-cavity centrelines (MX) and (MY).

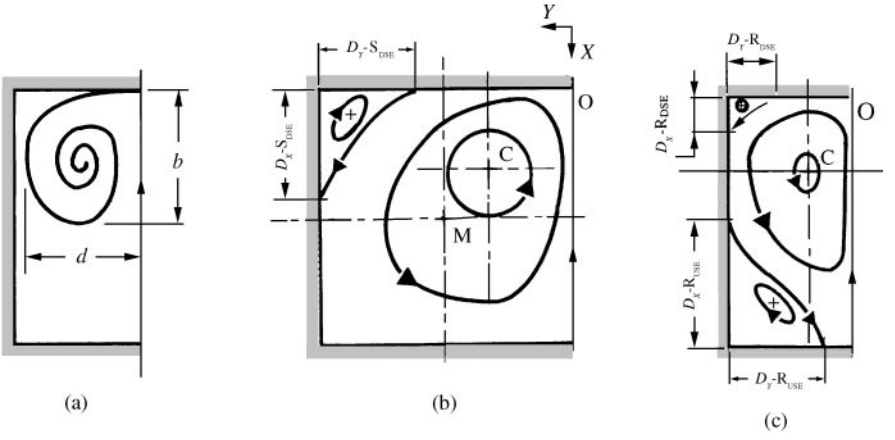

Figure 6. Cavity-eddy topological parameters: (a) dye-filament dimensions; (b) square-cavity flow parameters; (c) rectangular-cavity flow parameters.

3.2. Flow Topological Analysis

3.2.1. Dye-filament analysis, vorticity propagation approach

A qualitative examination of Figure 4 shows great influence of the cavity shape on vorticity propagation, in particular beyond $t^* = 2$. Up to $t^* = 6$, the square-cavity visualizations clearly reveal the free time development of the recirculation cell with no visible lateral-wall effects: a regular rounded rolling-up filament develops. Beyond $t^* = 6$, close to the cavity upper corner, a lid-wall effect scarcely deforms this constant rolling-up filament. However, up to $t^* = 12$, with no appreciable effect on its stretch: the rolling-up filament keeps a roughly constant value of about 0·9 [Figure 7(a)]. In opposition, for the other two confined cavity shapes (rectangular and semi-circular), the rolling-up filament elongates in the opposite direction of the lid motion (Figure 4); two development phases can therefore be distinguished. First, for $0 \leq t^* < 6$, the rectangular cell elongates under the cavity bottom-wall constraint, a quasi-linear time evolution of the stretch is to be noted with upper values for the more confined semi-circular cavity [figure 7(a)]. Secondly, beyond $t^* = 6$, a sharp increase of the stretch is observed [figure 7(a)]. This phenomenon is clearly identifiable on picture sequences by an elongation of the dye filament into a tip development for the semi-circular cavity and, markedly, for the rectangular one (Figure 4). In fact, from $t^* = 6$, the elongation phenomenon is governed by the attraction of the low-pressure area which prevails at the foot of the cavity and, in addition for the rectangular case, by the development of the rectangular$_{USE}$ which flattens the main recirculation zone (described below).

For the three cavity shapes, the dimensionless area of the dye filament displays a similar time development up to $t^* = 2$, and even up to $t^* = 4$ for the square and rectangular cavities, even though, strong differences of the recirculation-zone shape exist [figure 7(b)]. Beyond those time values, the dye-filament area of the square cavity always progresses linearly whereas, for the other two confining cavity shapes, this progress is markedly slowing in a quasi-parabolic evolution. This shows that the mass dispersion process in the square cavity is more efficient. At the final time stage ($t^* = 12$), the semi-circular- and the rectangular-cavity dye-filament areas, respectively, represent 56 and 62% of the square-cavity dye-filament one. On the other hand, dye visualizations reveal that the

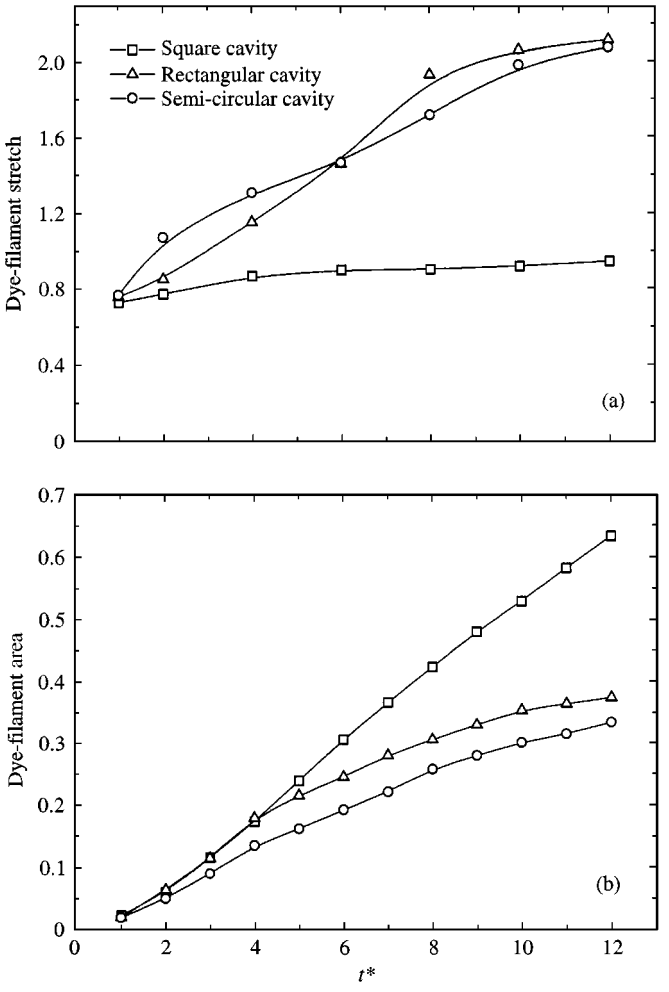

Figure 7. Comparative evolution of (a) dye-filament stretch and (b) area.

semi-circular-cavity dye filament tends to completely "fill" the whole available area, so as to fit well the cavity shape (Figure 4). At the final time stage, 90% of the whole semi-circular-cavity area is affected by the main recirculation whereas, 74% and only 63% of the rectangular- and square-cavity areas are, respectively, concerned. Thus, the semi-circular cavity results in a much more homogeneous and uniform recirculation, leading to a better efficiency in the early time stages of the mixing process, even though, as previously shown, it is less effective in mass dispersion.

3.2.2. Primary and secondary eddy characteristics: streamline analysis

Solid tracer visualizations analysis leads to additional topological flow details (Figure 5). Cavity flow comparisons show that the depth-to-width ($D : B$) aspect ratio has an important influence on the PE penetration (Figure 8). At flow start ($1 \leq t^* \leq 2$), the three cavity flows PE-core coordinates are close and go along the square cavity diagonal line. With time, the $\text{square}_{\text{PE}}$ core continues to follow this diagonal, moving towards the square cavity

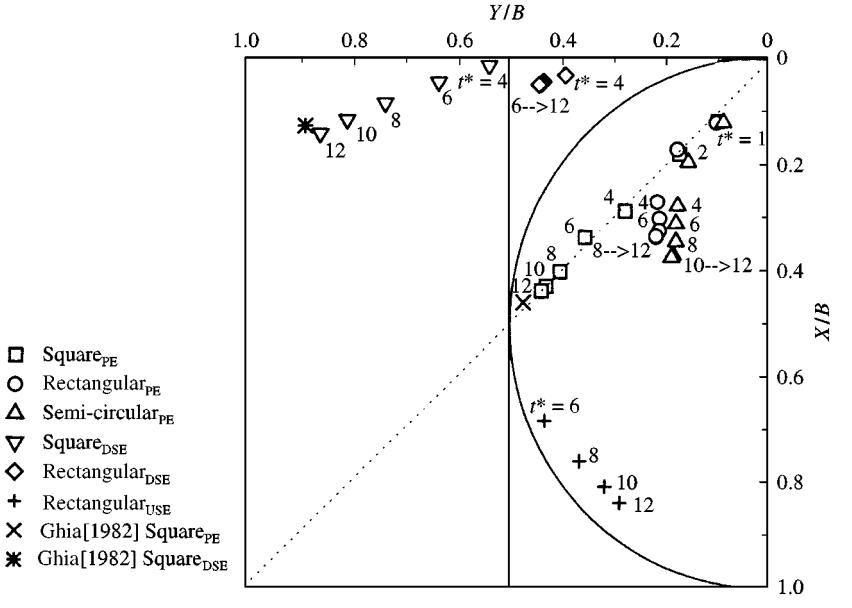

Figure 8. Primary and secondary vortex-core trajectories.

geometric centre (at $t^* = 12$, X-square$_{PE}$ = Y-square$_{PE}$ = 0·44B), relatively close to the steady value obtained by Ghia *et al.* (1982). In opposition, beyond $t^* = 2$, due to the bottom-wall constraint, the other two cavity flow vortex cores deviate, following, up to $t^* = 8$–10, a linear evolution parallel to the lid (Y-rectangualr$_{PE}$ = 0·21 and Y-semi-circular$_{PE}$ = 0·18). Next, up to the final time, they roughly remain steady (X-rectangular$_{PE}$ = 0·34B and X-semi-circular$_{PE}$ = 0·37B).

As mentioned above (Section 3.1), the square- and rectangular-cavity flows generate secondary eddies. During the explored establishment phase ($0 \leq t^* \leq 12$), only one secondary eddy forms in the square cavity (Figure 5). Since $t^* = 4$, in a magnified picture, this eddy is visible close to the downstream-wall mid-point. With time, it slowly enlarges and moves to the downstream corner to form, in standard literature notation, the DSE (occupying approximately 8% of the square-cavity area at $t^* = 12$). In a numerical study, Gustafson & Halasi (1986) described a similar wall-eddy migration phenomenon for cavities of depth-to-width aspect ratio greater than 1·5 and for a Reynolds number of 800. In their case, the wall eddy moves to the downstream corner and coalesces with an already formed DSE. After coalescence, a unique DSE was observed. Does this initial DSE exist in the present experiments? Its presence is a distinct possiblility, but, due to the downstream-corner velocities and the relativelly small eddy size, it is not visible in the visualizations. As shown in Figure 8, during the whole time sequence, the trajectory of the square$_{DSE}$ core is quasi-linear and, at the final time stage ($t^* = 12$), it takes place, as the primary eddy core, close to the steady state value obtained in the 2-D numerical study of Ghia *et al.* (1982), which seems to bring out that the fully established coordinates of the square$_{DSE}$ core are almost reached as early as $t^* = 12$.

Details on time evolution of square$_{DSE}$ dimensions (D_Y-square$_{DSE}$ and D_X-square$_{DSE}$) are given in Figure 9(a). After a D_y-square$_{DSE}$ decrease and a D_x-square$_{DSE}$ increase, these eddy dimensions seem to reach steady values (D_X-square$_{DSE}$ $\approx$ D_Y-square$_{DSE}$ $\approx$ 0·39B). Oddly, at $t^* = 12$, the D_Y-square$_{DSE}$ value is in better agreement with the steady 2-D numerical results

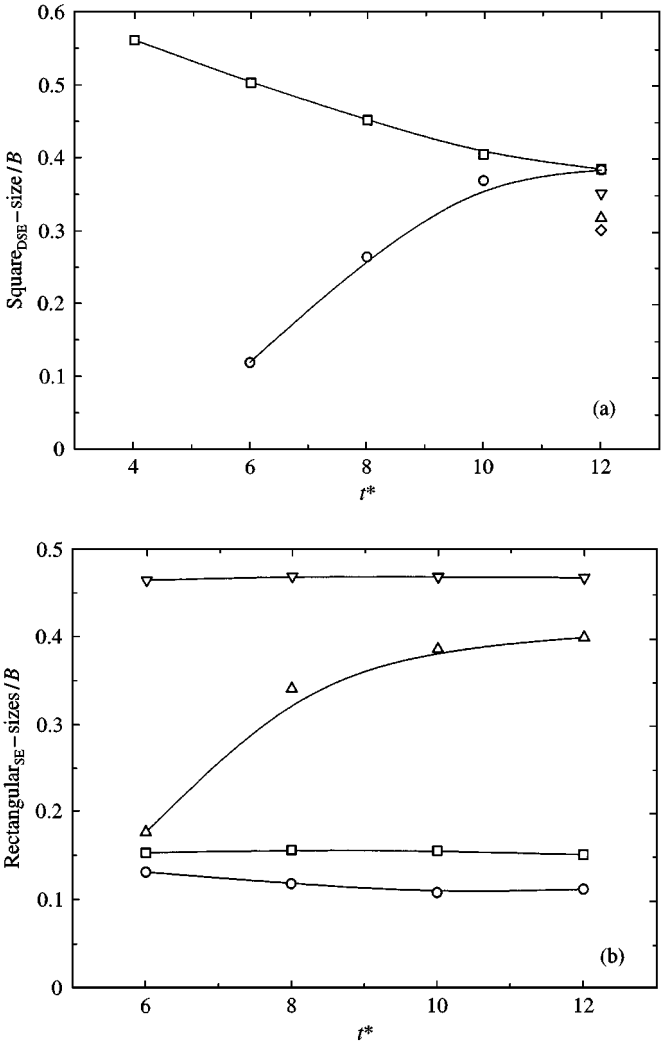

Figure 9. Secondary eddy size time evolutions: (a) square cavity: –□–, D_y-Square$_{DSE}$; –○–, D_x-Square$_{DSE}$; △, Koseff (1984a,b,c) D_Y-Square$_{DSE}$; ▽, Ghia *et al.* (1982) D_Y-Square$_{DSE}$; ◇, Ghia *et al.* (1982) D_X-Square$_{DSE}$; (b) rectangular cavity: –□–, D_Y-Rectangular$_{DSE}$; –○–, D_X-Rectangular$_{DSE}$; –△–, D_Y- Rectangular$_{USE}$; –▽–, D_X.-Rectangular$_{USE}$.

of Ghia *et al.* (1982) than the experimental ones of Koseff & Street (1982). We assume that even if, at $t^* = 12$ cross-sectional structures seem to come up to steady state, the whole 3-D characteristics of cavity flow are certainly not fully developed, especially Taylor-Goezther like vortices which could alter the characteristics of the cross-section flow visualized and especially the square$_{DSE}$ dimensions.

In the rectangular-cavity case, two secondary eddies form. On pictures, the rectangular$_{DSE}$ becomes visible as early as $t^* = 4$, and as could be seen in Figures 8 and 9(b), from $t^* = 6$, its state keeps steady (except a slender D_X-rectangular$_{DSE}$ decrease) and its area stays in the order of 2% of the rectangular-cavity area [D_Y-rectangular$_{DSE} = 0{\cdot}15B$, D_X-rectangular$_{DSE} = 0{\cdot}11B$ and (X-rectangular$_{DSE}$, Y-rectangular$_{DSE}$) = $(0{\cdot}05B, 0{\cdot}44B)$]. From $t^* = 6$,

another rectangular-cavity secondary eddy (rectangular$_{USE}$), larger than the previous rectangular$_{DSE}$ one, appears along the bottom-wall foot. With time, this rectangular$_{USE}$ grows until it occupies approximately 21% of the total rectangular-cavity area. During its development phase, and up to $t^* = 12$, the rectangular$_{USE}$ core moves linearly as to be located in an (X-rectangular$_{USE}$, Y-rectangular$_{USE}$) coordinates of ($0{\cdot}84B, 0{\cdot}29B$). During this whole time sequence, the rectangular$_{USE}$-separated point (on the bottom wall) remains steady (D_X-rectangular$_{USE} = 0{\cdot}47B$) whereas the reattached-point location (on the upstream wall) moves with time in a parabolic evolution so as to reach, from $t^* = 10$, a stationary value of about $0{\cdot}40B$ (Figure 9b). Unfortunately, no results on the rectangular-cavity flow have been found in the literature to make comparisons and even validate or invalidate this experimental outcome.

3.3. Flow Kinematic Analysis

A kinematic flow illustration, stemming from the analysis of solid-tracer visualizations, is given in Figure 10. The measured dimensionless V_x- and V_y-velocity profiles normalized by the lid velocity, taken along the reference vertical and horizontal square-cavity centrelines (MX and MY) are plotted at selected consecutive time-stages. The obvious result arising from this drawing is that the profile shapes differ over the whole time-sequence, showing the kinematic flow unsteadiness due to the progressive development of the primary eddy. However, from $t^* = 8$, velocities seem to reach their steady state in the upper and right parts of the respective vertical and horizontal profiles. At the final stage ($t^* = 12$), comparison between the experimental velocity profiles and the 2-D numerical ones of Ghia *et al.* (1982) leads to an almost good agreement in shape but not in value, which illustrates the 3-D character of the flow in the experiments. Indeed, as shown by Koseff & Street (1984a–c), three-dimensional perturbations, coming from the cavity-span ends, weakened the mid-cross-section flow velocities compared to the purely 2-D configuration. In the present experiments, as shown in Figure 11, 3-D flow structures were effectively visualized but, as mentioned above, are certainly not fully developed at the last dimensionless time shown ($t^* = 12$). New experiments focusing on time evolution of these 3-D perturbations are in progress.

To allow direct velocity comparisons between the three cavity shapes, the V_x- and V_y-velocity profiles along each primary vortex-core centrelines (CX and CY), are given in Figures 12–15. Figures 12–14 show time evolution of the velocity profiles in the respective square, rectangular and semi-circular cavities. Figure 15 shows comparison between velocity profiles of the three cavities for two selected time stages ($t^* = 2$ and 12). In the rectangular- and semi-circular-cavity cases the PE reaches its kinematic steady state as early as $t^* = 6$ on the horizontal axis, and respectively at $t^* = 8$ and 10 in the vertical direction. On the contrary, in the square-cavity case, vertical and horizontal profiles evolve up to the final time, but from $t^* = 10$ to 12 a quasi-steady state emerges associated with only slight evolution of the profiles. However, it might be strange to observe such a phenomenon whereas, as previously shown (Figure 10), the upper and right parts of the respective vertical and horizontal cavity centreline (MX and MY) profiles seem to remain steady from as early as $t^* = 8$. This difference simply arises from the reference shapes used to draw the profiles. Indeed, in the upper and right parts of the square cavity, the kinematic flow is effectively quasi-steady from $t^* = 8$; but, in the vortex-core centrelines, due to the progression of the primary eddy vortex core (Figure 8), profiles continue to evolve, and they are still offset, up to $t^* = 12$. It is also noteworthy that for the three cavities, the quasi-linearity of the velocities in the vortex-core region is indicative of uniform vorticity

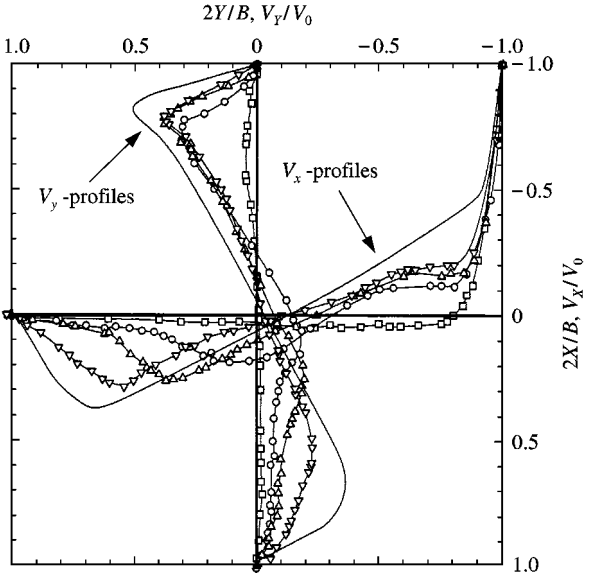

Figure 10. V_x- and V_y-velocity profile time evolutions along the respective square cavity horizontal and vertical centrelines: –□–, $t^* = 2$; –○–, $t^* = 6$; –△–, $t^* = 8$; –▽–, $t^* = 12$; ——, Ghia *et al.* (1982).

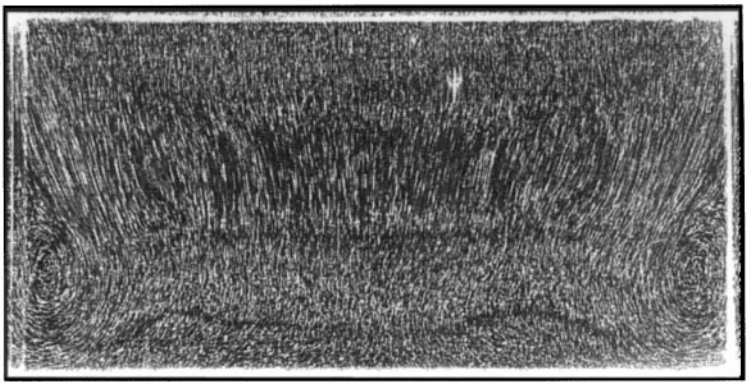

Figure 11. Square-cavity spanwise visualization ($Y/D = \frac{1}{2}$), $t^* = 12$.

distribution (Migeon *et al.* 1998) or, at least, of weak vorticity gradient as previously reported in Ghia's (1982) study.

Comparison between velocity profiles [Figures 15(a)], through the three cavity vortex-core centrelines, clearly confirm that even though the cavity shape acts, as previously shown [Figure 7(a)], on the first stages of flow development, kinematic similarities are noticeable. Indeed, as early as $t^* = 2$ the velocity profile comparison between the three cavities is quite good; even so, differences appear close to the horizontal axis velocity extrema representing the first signs of cavity shape influence. With evolving time, as shown in Figure 15(b), both rectangular- and semi-circular cavity vertical and horizontal profiles remain roughly identical. On the contrary, the square cavity ones, especially marked for the V_x-profile, separate from the other two, pointing to the rising effect, with time, of cavity depth. In the

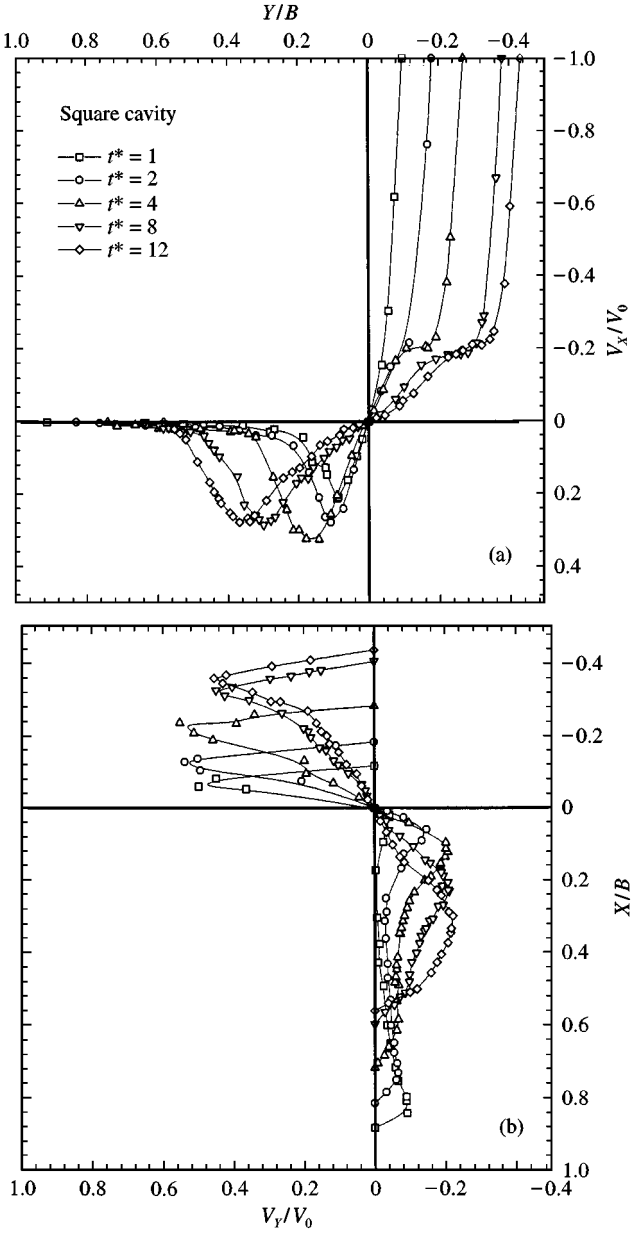

Figure 12. (a) V_x- and (b) V_y-velocity profile time evolutions along the respective square cavity horizontal and vertical vortex-core centrelines.

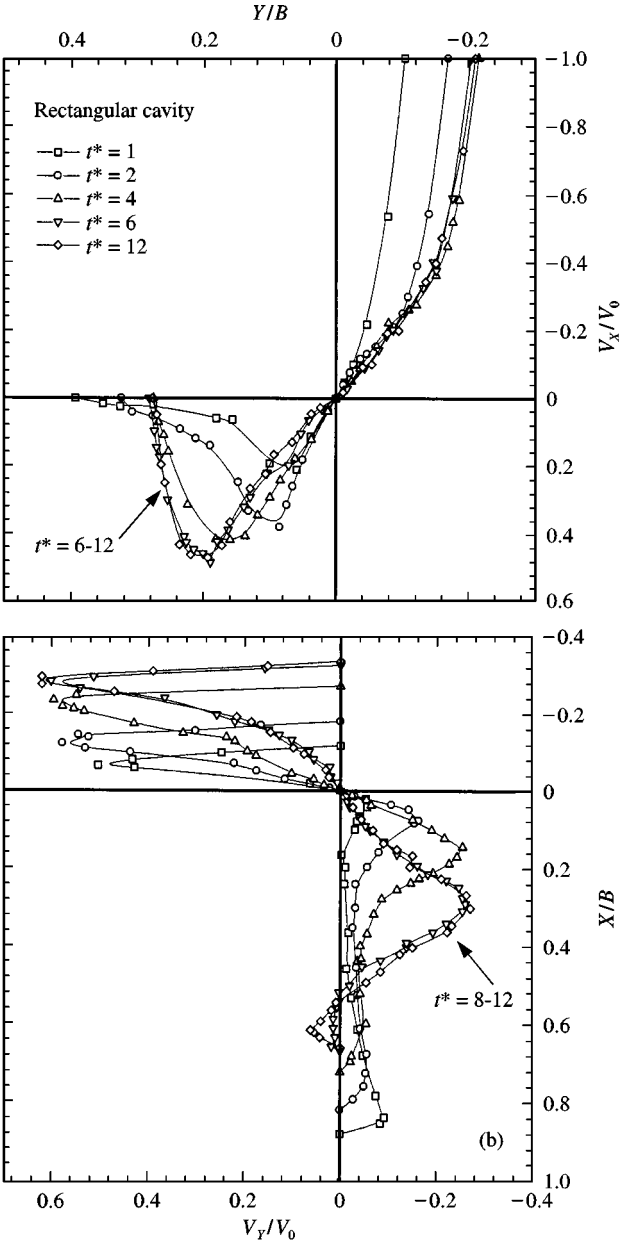

Figure 13. (a) V_x- and (b) V_y-velocity profile time evolutions along the respective rectangular cavity horizontal and vertical vortex-core centrelines.

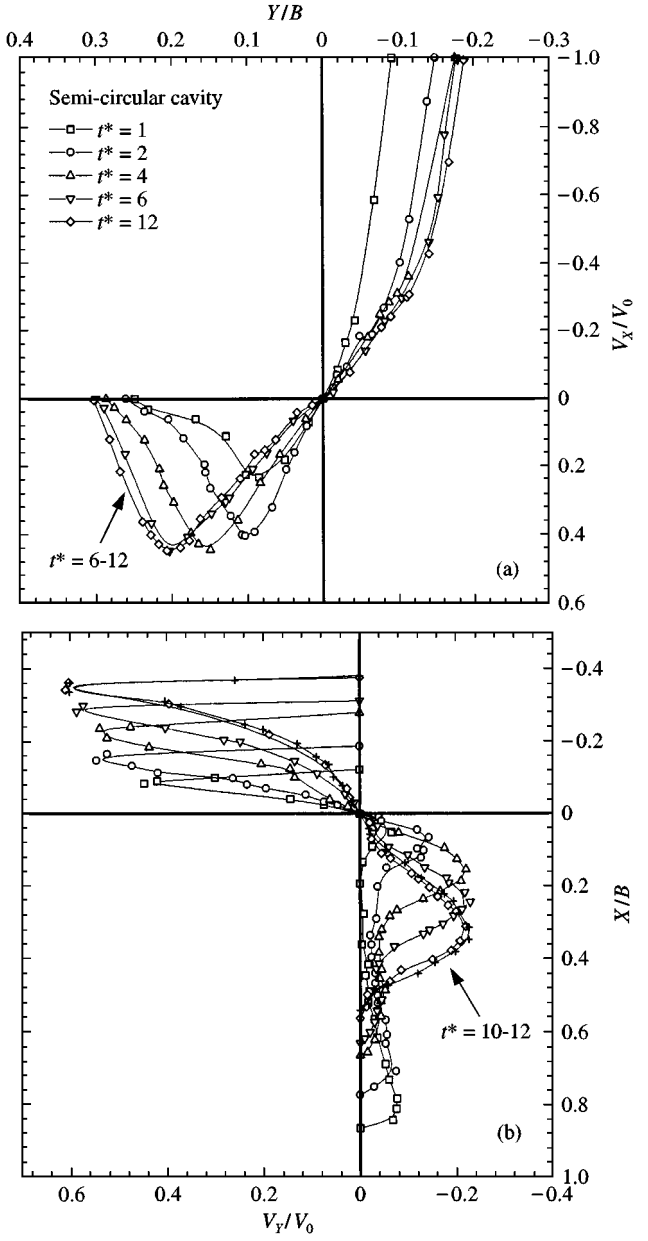

Figure 14. (a) V_x- and (b) V_y-velocity profile time evolutions along the respective semi-circular cavity horizontal and vertical vortex-core centrelines.

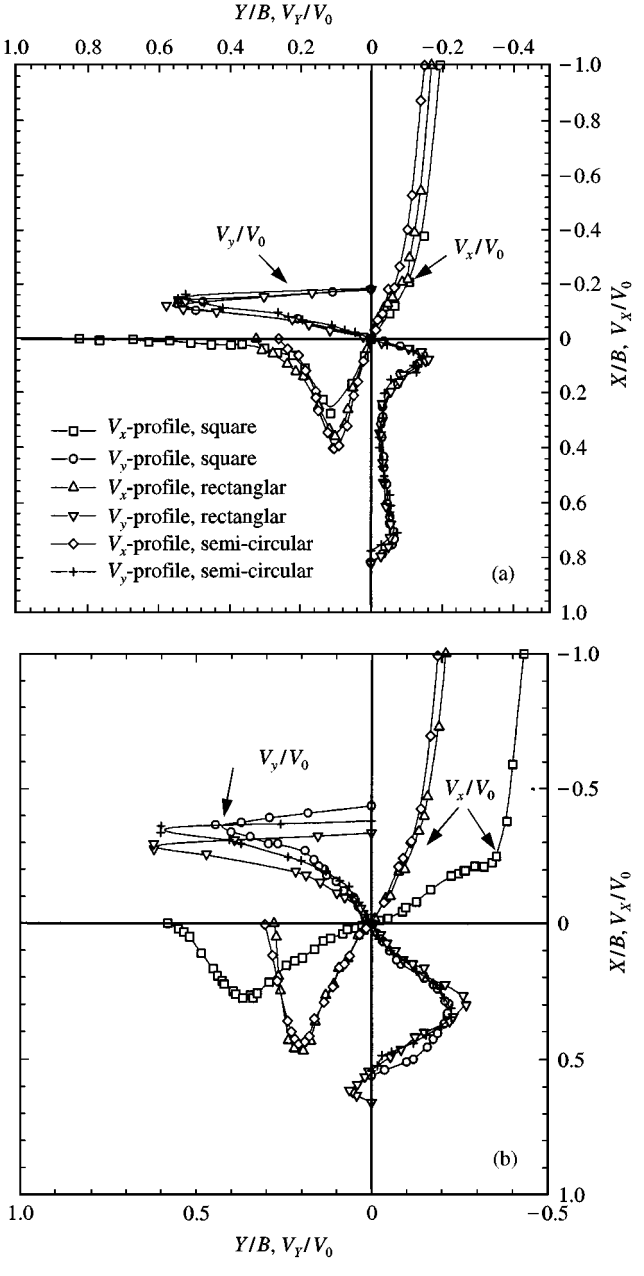

Figure 15. V_x- and V_y-velocity profile comparisons along the three cavity vortex-core centrelines for two time stages: (a) $t^* = 2$ and (b) $t^* = 12$.

horizontal direction (V_x profiles), due to the cavity confined area, the velocity gradients in rectangular and semi-circular cavities are steeper than the square-cavity ones. Thus, the vorticity magnitude in the eddy-core region is greater for the rectangular and semi-circular cavities.

4. CONCLUSION

Novel hydrodynamic simulations have been made to fill the shortfall of references on the detailed birth of lid-driven cavity flows. Three standard manufactured cavity shapes have been considered and compared: a square one, a rectangular one and a semi-circular one. The studied cavity is translated downward along a fixed vertical lid; flow pictures are recorded at regular time stages ($0 \leq t^* \leq 12$) by means of an accompanying camera, so that the cavity seems to be fixed and the lid appears as the moving cavity wall. Two complementary visualization techniques give fine topological and kinematic information on the mixing process, vorticity propagation and on the precise location of vortex cores and of divided and reattached points.

It is shown that in the first time stages the cavity geometry (with the same cavity opening) has a significant effect on flow structure development, even if kinematic similarities exist. Among the three cavity flows studied, the semi-circular one results in a much more homogeneous and uniform recirculation with no low-velocity secondary eddies; only one main eddy develops. For the two parallelepipedic cavities, the process of secondary eddies birth and development is clearly shown. In the short time sequence investigated, unlike the fully developed regime, the square-cavity flow develops only one secondary eddy which forms on the downstream wall and then merges to the downstream corner to form the so-termed downstream secondary eddy, which occupies 8% of the square-cavity area. In the rectangular cavity case, two secondary eddies form, one close to the cavity downstream-corner and the other close to the cavity upstream corner; they respectively occupy 2 and 21% of the total rectangular cavity area. From both topological and kinematic investigations, it clearly appears that the two more confined cavity flows (semi-circular and rectangular) reached a quasi-steady state from $t^* = 8$–10 (stagnation of vortex-core positions, secondary eddy sizes and velocity profiles). For the square-cavity case, even though at the final time stage steady flow is reached in the upper cavity part (stagnation of secondary eddy sizes and velocity profiles), the flow is still evolving in the cavity foot zone, especially close to the upstream and bottom walls. Moreover, in the square-cavity case, differences observed between computing and experiment point out the emergence of 3-D perturbations.

New experiment are now in progress to investigate in detail the birth of 3-D flow features by taking into consideration visualization in different spanwise views, variable cavity lengths and for different cavity lid speeds.

References

Aidun, C. K. & Triantafillopoulos, N. G. 1990 In *International Symposium on Mechanics of Thin-film Coating*, Spring National Meeting of the AIChE.

Aidun, C. K., Triantafillopoulos, N. G. & Benson, J. D. 1991 Global stability of a lid-driven cavity with throughflow: flow visualization studies. *Physics of Fluids* **A3,** 2081–2090.

Boisaubert, N., Coutanceau, M. & Ehrmann, P. 1996 Comparative early development of wake vortices behind a short semicircular-section cylinder in two opposite arrangements. *Journal of Fluid Mechanics* **327,** 73–99.

Chiang, T. P., Hwang, R. R. & Sheu, W. H. 1997 On end-wall corner vortices in a lid-driven cavity. *ASME Journal of Fluids Engineering* **119,** 201–204.

Deville, M., Thien-Hiep Lê Morchoisne, Y. 1992 GAMM-Workshop, Vieweg.
Freitas, C. J., Street, R. L., Findikakis, A. N. & Koseff, J. R. 1985 Numerical simulation of three-dimensional flow in a cavity. *International Journal for Numerical Methods in Fluids* **5,** 561–575.
Freitas, C. J. & Street, R. L. 1988 Non-linear transient phenomena in a complex recirculating flow: a numerical investigation. *International Journal for Numerical Methods in Fluids* **8,** 669–801.
Ghia, U., Ghia, K. N. & Shin, C. T. 1982 High-Re solutions for incompressible flow using the Navier-Stokes equations and a Multigrid method. *Journal of Computational Physics* **48,** 387–411.
Gustafson, K. & Halasi, K. 1986 Vortex dynamics of cavity flows. *Journal of Computational Physics* **64,** 279–319.
Koseff, J. R. & Street, R. L. 1982 Visualization studies of a shear driven three-dimensional recirculating flow. In *Proceedings Thermophysics and Heat transfer Conference on Three*-Dimensional Turbulent Shear Flows, AIAA/ASME, St Louis, pp. 23–31.
Koseff, J. R. & Street, R. L. 1984a Visualization studies of a shear driven three-dimensional recirculating flow. *ASME Journal of Fluids Engineering* **106,** 21–29.
Koseff, J. R. & Street, R. L. 1984b On end wall effects in a lid-driven cavity flow. *ASME Journal of Fluids Engineering* **106,** 385–389.
Koseff, J. R. & Street, R. L. 1984c The lid-driven cavity flow: a synthesis of qualitative and quantitative observations. *ASME Journal of Fluids Engineering* **106,** 390–398.
Ramanan, N. & Homsy, G. M. 1994 Linear stability of lid-driven cavity flow. *Physics of Fluids* **6,** 2690–2701.
Middleman, S. 1977 *Fundamentals of Polymer Processing*. New York: McGraw Hill.
Pan, F. & Acrivos, A. 1966 Steady flows in rectangular cavities. *Journal of Fluid Mechanic* **23,** 643–655.
Migeon, C., Aubert, S., Texier, A. & Ferrand, P. 1998 Vorticity generation and transport inside a square lid-driven cavity: numerical and experimental investigations. *Third International Workshop on Vortex flows and Related Numerical Methods*, pp. 175–176.
Prasad, A. K. & Koseff, J. R. 1988 Reynolds number and end-wall effects on a lid-driven cavity flow. *Physics of Fluids* **A1,** 208–218.

APPENDIX: Nomenclature

A, $A_{\text{dye-filament}}$, A_s	dimensionless dye-filament area, delimited dye-filament area, and square-cavity area
B	cavity width
CX, CY	primary eddy centrelines
d, b	depth-, width-space of the dye-filament rolling-up
D	cavity depth
DSE	downstream secondary eddy
D_x, D_y	secondary eddy size on X-, Y-axis
L	cavity length
LDC	lid-driven cavity
MX, MY	square-cavity centrelines
PE	primary eddy
Re	Reynolds number, $\text{Re} = V_0 B/\nu$
SE	secondary eddy
S_{th}	dimensionless dye-filament stretch
t^*	dimensionless time, $t^* = tV_0/B$
USE	Upstream secondary eddy
V_0	constant velocity lid
V_x, V_y	velocity component along X-, Y-axis
X, Y	vortex-core coordinates
ν	fluid kinematic viscosity

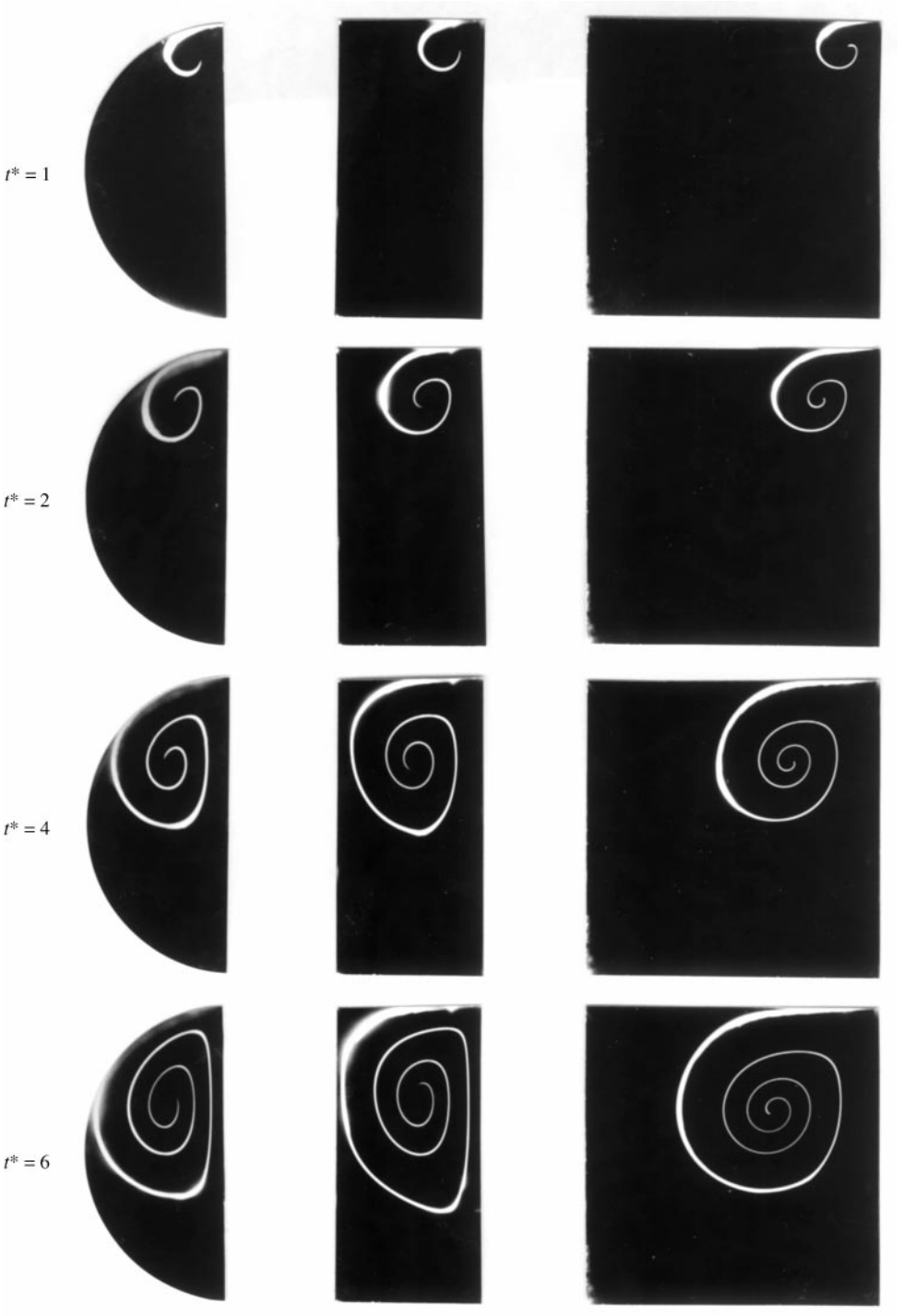

Figure 4. Dye filament time evolutions; comparison between cavities.